INTERNATIONAL JOURNAL FOR NUMERICAL METHODS IN FLUIDS
Int. J. Numer. Meth. Fluids 2006; **50**:1425–1444
Published online 15 November 2005 in Wiley InterScience (www.interscience.wiley.com). DOI: 10.1002/fld.1105

Numerical modelling of 3D stratified free surface flows: a case study of sediment dumping

Pengzhi Lin[1,2,*,†,‡] and Dongchao Wang[2]

[1]*State Key Laboratory of Hydraulics and River Mountain Engineering, Sichuan University, People's Republic of China*
[2]*Department of Civil Engineering, National University of Singapore, Singapore 117576, Singapore*

SUMMARY

A three-dimensional numerical model has been developed to simulate stratified flows with free surfaces. The model is based on the Reynolds-averaged Navier–Stokes (RANS) equations with variable fluid density. The equations are solved in a transformed σ-coordinate system with the use of operator-splitting method (*Int. J. Numer. Meth. Fluids* 2002; **38**:1045–1068). The numerical model is validated against the one-dimensional diffusion problem and the two-dimensional density-gradient flow. Excellent agreements are obtained between numerical results and analytical solutions. The model is then used to study transport phenomena of dumped sediments into a water body, which has been modelled as a strongly stratified flow. For the two-dimensional problem, the numerical results compare well with experimental data in terms of mean particle falling velocity and spreading rate of the sediment cloud for both coarse and medium-size sediments. The model is also employed to study the dumping of sediments in a three-dimensional environment with the presence of free surface. It is found that during the descending process an annulus-like cloud is formed for fine sediments whereas a plate-like cloud for medium-size sediments. The model is proven to be a good tool to simulate strongly stratified free surface flows. Copyright © 2005 John Wiley & Sons, Ltd.

KEY WORDS: 3D numerical model; stratified flows; free surface; sediment dumping; Navier–Stokes equations solver

1. INTRODUCTION

Complex stratified flows are encountered in natural processes and engineering practices, in which non-uniform distribution of temperature, solute concentration (e.g. salinity), air bubble or suspended particle (e.g. sediment) exists. The non-uniformity of these physical variables

*Correspondence to: Pengzhi Lin, Department of Civil Engineering, National University of Singapore, Singapore 117576, Singapore.
†E-mail: cvelinpz@nus.edu.sg
‡Associate Professor.

Contract/grant sponsor: National University of Singapore; contract/grant number: WBS: R-264-000-136-112

Received 9 January 2004
Revised 4 November 2004
Accepted 20 August 2005

reveals themselves through the change of effective fluid density. The studies of stratified flows are especially important in estuarial and coastal regions, where density stratification can be induced by many natural or man-made processes. Examples include sediment-laden flows above seabed, wave-river flow interaction in estuaries, internal waves on the continental shelf, buoyant plumes and jets around marine outfalls and sediment dumping by barges.

Conventionally, stratified flows are solved with Boussinesq assumption (e.g. Reference [1]). Boussinesq assumption can simplify the problem but its validity relies on the physical condition of weak stratification. However, it has been observed [2] experimentally that for a non-Boussinesq case, where the initial density difference between the plume and ambient flow is large, the entrainment velocity partly depends on the ratio of the plume density to the ambient fluid density. The recent work of Woods [3] suggested that non-Boussinesq effects may have a great impact on the shape and density evolution of a plume over a certain distance above the source. Thus, for strong flow stratification, the direct solution to the Navier–Stokes equations (NSE) without Boussinesq assumption should be used to provide more accurate results.

There are a few numerical models that solved NSE with varying density, most of which, however, were for 2D flows. For example, Gu [4], by using a 2D unsteady model, examined submerged warm turbulent buoyant jets in a stratified lake or reservoir with an ice cover; Liu *et al.* [5] simulated the salinity field and tidal current by 2D models with different types of turbulence closure models; Shen *et al.* [6] used a turbulent two-phase flow model to simulate turbulent stratified flows.

In recent years, several 3D models for stratified flows have been developed, all of which, however, employed either the Boussinesq approximation (e.g. References [7–12]) for weakly stratified flows or hydrostatic pressure assumption that restrict the application to long waves only (e.g. References [8, 13, 14]).

The 3D numerical model that solves the original NSE or its kind for stratified free surface flows has rarely been reported. In this paper, we will present a 3D numerical model for general stratified free surface flows, in which neither Boussinesq assumption nor hydrostatic pressure assumption is employed. The model is the extension of the earlier model developed by Lin and Li [15] who solved NSE in σ-coordinate for constant density fluids. By introducing density variation, a transport equation for fluid density is solved by the cubic-interpolated propagation (CIP) method developed by Yabe *et al.* [16]. The CIP method has the advantage of capturing the moving sharp interface front. The developed model will be validated for various stratified flow problems that will be detailed in the later sections.

2. GOVERNING EQUATIONS

For a 3D incompressible stratified flow, the governing equations are NSE. For turbulent flows, NSE can be transformed into Reynolds-averaged Navier–Stokes (RANS) equations by taking the ensemble average of the original equations. The resulting equations are

$$\frac{\partial u_I}{\partial x_I^*} = 0 \tag{1}$$

$$\frac{\partial u_I}{\partial t^*} + u_J \frac{\partial u_I}{\partial x_J^*} = -\frac{1}{\rho}\frac{\partial p}{\partial x_I^*} + g_I + \frac{1}{\rho}\frac{\partial \tau_{IJ}}{\partial x_J^*} \tag{2}$$

where $I,J = 1,2,3$, u_I is the mean velocity component in the Ith direction, p the mean pressure, ρ the mean density, and

$$\tau_{IJ} = \rho(\nu + \nu_t)\left(\frac{\partial u_I}{\partial x_J^*} + \frac{\partial u_J}{\partial x_I^*}\right)$$

the combinations of the molecular viscous stresses and turbulent Reynolds stresses, where ν is the kinematic molecular viscosity and ν_t kinematic eddy viscosity.

The mean fluid density ρ in Equation (1) can be described by the scalar transport equation as

$$\frac{\partial \rho}{\partial t^*} + (u_J + u_{TJ})\frac{\partial \rho}{\partial x_J^*} = \frac{\partial}{\partial x_J^*}\left(\Gamma_t \frac{\partial \rho}{\partial x_J^*}\right) \tag{3}$$

where $\Gamma_t = \nu_t/\sigma_t$ is the turbulent diffusivity for ρ with σ_t being the turbulent Schmidt number. $(u_{T1}, u_{T2}, u_{T3}) = (0, 0, -w_\mathrm{d})$ is the drift velocity for non-dissolving substances (e.g. air bubble, sediment) that represent the additional separation velocity of substance from its mean plume. The determination of the drift velocity w_d and eddy viscosity ν_t/Γ_t depends upon the flow type and will be detailed when case studies are made. It is noted that for solute in a laminar flow, Equation (3) can be reduced to $(\partial\rho/\partial t^*) + u_J(\partial\rho/\partial x_J^*) = 0$, the original incompressibility condition for fluid.

The governing equation for the free surface displacement can be obtained by integrating vertically the continuity Equation (1) with appropriate boundary conditions:

$$\frac{\partial \eta}{\partial t^*} + \frac{\partial}{\partial x_J^*}\int_{-h}^{\eta} u_J \, \mathrm{d}z^* = 0 \tag{4}$$

where $J = 1,2$ and η is the surface displacement.

3. COORDINATE TRANSFORMATION AND NUMERICAL PROCEDURES

3.1. Coordinate transformation

The numerical discretization used in the study is similar to that in Reference [15], and thus it is only described here briefly. First, the σ-coordinate transformation is introduced that would map the irregular computation domain to a regular computational domain. Assuming the free surface is the single function of the horizontal plane, a σ-coordinate, which is modified from Blumberg and Mellor's [17] original proposal, is introduced as follows:

$$t = t^*, \quad x = x^*, \quad y = y^*, \quad \sigma = \frac{z^* + h}{D} \tag{5}$$

where h is still water depth and $D=\eta+h$. Substituting the above definition into the governing Equations (1)–(3), we obtain

$$\frac{\partial u}{\partial x}+\frac{\partial u}{\partial \sigma}\frac{\partial \sigma}{\partial x^*}+\frac{\partial v}{\partial y}+\frac{\partial v}{\partial \sigma}\frac{\partial \sigma}{\partial y^*}+\frac{\partial w}{\partial \sigma}\frac{\partial \sigma}{\partial z^*}=0 \tag{6}$$

$$\begin{aligned}&\frac{\partial u}{\partial t}+u\frac{\partial u}{\partial x}+v\frac{\partial u}{\partial y}+\omega\frac{\partial u}{\partial \sigma}\\&\quad=-\frac{1}{\rho}\left(\frac{\partial p}{\partial x}+\frac{\partial p}{\partial \sigma}\frac{\partial \sigma}{\partial x^*}\right)+g_x\\&\qquad+\frac{1}{\rho}\left(\frac{\partial \tau_{xx}}{\partial x}+\frac{\partial \tau_{xx}}{\partial \sigma}\frac{\partial \sigma}{\partial x^*}+\frac{\partial \tau_{xy}}{\partial y}+\frac{\partial \tau_{xy}}{\partial \sigma}\frac{\partial \sigma}{\partial y^*}+\frac{\partial \tau_{xz}}{\partial \sigma}\frac{\partial \sigma}{\partial z^*}\right)\end{aligned} \tag{7}$$

$$\begin{aligned}&\frac{\partial v}{\partial t}+u\frac{\partial v}{\partial x}+v\frac{\partial v}{\partial y}+\omega\frac{\partial v}{\partial \sigma}\\&\quad=-\frac{1}{\rho}\left(\frac{\partial p}{\partial y}+\frac{\partial p}{\partial \sigma}\frac{\partial \sigma}{\partial y^*}\right)+g_y\\&\qquad+\frac{1}{\rho}\left(\frac{\partial \tau_{yx}}{\partial x}+\frac{\partial \tau_{yx}}{\partial \sigma}\frac{\partial \sigma}{\partial x^*}+\frac{\partial \tau_{yy}}{\partial y}+\frac{\partial \tau_{yy}}{\partial \sigma}\frac{\partial \sigma}{\partial y^*}+\frac{\partial \tau_{yz}}{\partial \sigma}\frac{\partial \sigma}{\partial z^*}\right)\end{aligned} \tag{8}$$

$$\begin{aligned}&\frac{\partial w}{\partial t}+u\frac{\partial w}{\partial x}+v\frac{\partial w}{\partial y}+\omega\frac{\partial w}{\partial \sigma}\\&\quad=-\frac{1}{\rho}\frac{\partial p}{\partial \sigma}\frac{\partial \sigma}{\partial z^*}+g_z\\&\qquad+\frac{1}{\rho}\left(\frac{\partial \tau_{zx}}{\partial x}+\frac{\partial \tau_{zx}}{\partial \sigma}\frac{\partial \sigma}{\partial x^*}+\frac{\partial \tau_{zy}}{\partial y}+\frac{\partial \tau_{zy}}{\partial \sigma}\frac{\partial \sigma}{\partial y^*}+\frac{\partial \tau_{zz}}{\partial \sigma}\frac{\partial \sigma}{\partial z^*}\right)\end{aligned} \tag{9}$$

$$\begin{aligned}&\frac{\partial \rho}{\partial t}+u\frac{\partial \rho}{\partial x}+v\frac{\partial \rho}{\partial y}+\omega_0\frac{\partial \rho}{\partial \sigma}\\&\quad=\frac{\partial}{\partial x}\left[\Gamma_t\left(\frac{\partial \rho}{\partial x}+\frac{\partial \rho}{\partial \sigma}\frac{\partial \sigma}{\partial x^*}\right)\right]\\&\qquad+\frac{\partial}{\partial y}\left[\Gamma_t\left(\frac{\partial \rho}{\partial y}+\frac{\partial \rho}{\partial \sigma}\frac{\partial \sigma}{\partial y^*}\right)\right]+\frac{\partial}{\partial z}\left[\Gamma_t\left(\frac{\partial \rho}{\partial \sigma}\frac{\partial \sigma}{\partial z^*}\right)\right]\end{aligned} \tag{10}$$

where

$$\omega=\frac{\partial \sigma}{\partial t^*}+u\frac{\partial \sigma}{\partial x^*}+v\frac{\partial \sigma}{\partial y^*}+w\frac{\partial \sigma}{\partial z^*}$$

$$\omega_0=\frac{\partial \sigma}{\partial t^*}+u\frac{\partial \sigma}{\partial x^*}+v\frac{\partial \sigma}{\partial y^*}+(w-w_{\mathrm{d}})\frac{\partial \sigma}{\partial z^*}$$

and,

$$\frac{\partial \sigma}{\partial t^*} = -\frac{\sigma}{D}\frac{\partial D}{\partial t}$$

$$\frac{\partial \sigma}{\partial x^*} = \frac{1}{D}\frac{\partial h}{\partial x} - \frac{\sigma}{D}\frac{\partial D}{\partial x}$$

$$\frac{\partial \sigma}{\partial y^*} = \frac{1}{D}\frac{\partial h}{\partial y} - \frac{\sigma}{D}\frac{\partial D}{\partial y}$$

$$\frac{\partial \sigma}{\partial z^*} = \frac{1}{D}$$

In the transformed space, the stresses are calculated as follows:

$$\begin{aligned}
\tau_{xx} &= 2\rho(\nu + \nu_t)\left(\frac{\partial u}{\partial x} + \frac{\partial u}{\partial \sigma}\frac{\partial \sigma}{\partial x^*}\right)\\
\tau_{yy} &= 2\rho(\nu + \nu_t)\left(\frac{\partial v}{\partial y} + \frac{\partial v}{\partial \sigma}\frac{\partial \sigma}{\partial y^*}\right)\\
\tau_{zz} &= 2\rho(\nu + \nu_t)\left(\frac{\partial w}{\partial \sigma}\frac{\partial \sigma}{\partial z^*}\right)\\
\tau_{xy} = \tau_{yx} &= \rho(\nu + \nu_t)\left(\frac{\partial u}{\partial y} + \frac{\partial u}{\partial \sigma}\frac{\partial \sigma}{\partial y^*} + \frac{\partial v}{\partial x} + \frac{\partial v}{\partial \sigma}\frac{\partial \sigma}{\partial x^*}\right)\\
\tau_{xz} = \tau_{zx} &= \rho(\nu + \nu_t)\left(\frac{\partial u}{\partial \sigma}\frac{\partial \sigma}{\partial z^*} + \frac{\partial w}{\partial x} + \frac{\partial w}{\partial \sigma}\frac{\partial \sigma}{\partial x^*}\right)\\
\tau_{yz} = \tau_{zy} &= \rho(\nu + \nu_t)\left(\frac{\partial v}{\partial \sigma}\frac{\partial \sigma}{\partial z^*} + \frac{\partial w}{\partial y} + \frac{\partial w}{\partial \sigma}\frac{\partial \sigma}{\partial y^*}\right)
\end{aligned} \tag{11}$$

The governing Equation (4) for the free surface movement is converted into

$$\frac{\partial \eta}{\partial t} + \frac{\partial}{\partial x}\left[D\int_0^1 u\,\mathrm{d}\sigma\right] + \frac{\partial}{\partial y}\left[D\int_0^1 v\,\mathrm{d}\sigma\right] = 0 \tag{12}$$

3.2. *Numerical procedures*

The numerical solution procedure adopted in this paper is on the basis of the operator-splitting method [15]. The introduction of variable density affects the numerical solution procedure. In the following sections, the numerical implementations will be summarized and the major changes that are caused by the density variation will be highlighted.

3.2.1. Convection step. In this section, the convection terms in the momentum equations from (7) to (9) are solved. Due to the similarity of these three equations, only Equation (7) is discussed here as well as in the diffusion step. The other two equations can be solved in the

same way. The corresponding finite difference form can be written as

$$\frac{u_{i,j,k}^{n+1/3}-u_{i,j,k}^{n}}{\Delta t}+\left(u\frac{\partial u}{\partial x}+v\frac{\partial u}{\partial y}+\omega\frac{\partial u}{\partial \sigma}\right)_{i,j,k}^{n}=0 \tag{13}$$

Since the density variation does not affect the convection term, the combination of quadratic backward characteristic method and Lax–Wendroff method as used by Lin and Li [15] is still applied in this step.

3.2.2. Diffusion step. The diffusion is solved following the convection step. In this step, the density variation needs to be treated properly when stresses are calculated. For instance, the corresponding finite difference scheme for Equation (7) reads

$$\frac{u_{i,j,k}^{n+2/3}-u_{i,j,k}^{n+1/3}}{\Delta t}=\frac{1}{\rho_{i,j,k}}\left(\frac{\partial \tau_{xx}}{\partial x}+\frac{\partial \tau_{xx}}{\partial \sigma}\frac{\partial \sigma}{\partial x^*}+\frac{\partial \tau_{xy}}{\partial y}+\frac{\partial \tau_{xy}}{\partial \sigma}\frac{\partial \sigma}{\partial y^*}+\frac{\partial \tau_{xz}}{\partial \sigma}\frac{\partial \sigma}{\partial z^*}\right)_{i,j,k}^{n+1/3} \tag{14}$$

All stress terms in the above equations can be calculated by using Equation (11). The central difference method is used to discretize all the partial differentiation terms in the above equation.

$$\left(\frac{\partial \tau_{xx}}{\partial x}\right)_{i,j,k}^{n+1/3}=\frac{(\tau_{xx})_{i+1/2,j,k}^{n+1/3}-(\tau_{xx})_{i-1/2,j,k}^{n+1/3}}{(\Delta x_{i-1}+\Delta x_i)/2}$$

where

$$(\tau_{xx})_{i+1/2,j,k}^{n+1/3}=2\nu\rho_{i+1/2,j,k}\left[\frac{u_{i+1,j,k}-u_{i,j,k}}{\Delta x_i}+\frac{u_{i+1/2,j,k+1}-u_{i+1/2,j,k-1}}{\Delta\sigma_{k-1}+\Delta\sigma_k}\left(\frac{\partial\sigma}{\partial x^*}\right)_{i+1/2,j,k}\right]^{n+1/3}$$

$$(\tau_{xx})_{i-1/2,j,k}^{n+1/3}=2\nu\rho_{i-1/2,j,k}\left[\frac{u_{i,j,k}-u_{i-1,j,k}}{\Delta x_{i-1}}+\frac{u_{i-1/2,j,k+1}-u_{i-1/2,j,k-1}}{\Delta\sigma_{k-1}+\Delta\sigma_k}\left(\frac{\partial\sigma}{\partial x^*}\right)_{i-1/2,j,k}\right]^{n+1/3}$$

3.2.3. Pressure-updating step. The pressure is updated by solving the Poisson pressure equation with the use of a sparse matrix solver such as conjugate gradient (CG) method as used by Lin and Li [15]. In this step, the pressure and body force on the right-hand side of Equations (7)–(9) are first discretized as follows:

$$\frac{u_{i,j,k}^{n+1}-u_{i,j,k}^{n+2/3}}{\Delta t}=-\frac{1}{\rho}\left(\frac{\partial p}{\partial x}+\frac{\partial p}{\partial \sigma}\frac{\partial \sigma}{\partial x^*}\right)_{i,j,k}^{n+1}+g_x \tag{15}$$

$$\frac{v_{i,j,k}^{n+1}-v_{i,j,k}^{n+2/3}}{\Delta t}=-\frac{1}{\rho}\left(\frac{\partial p}{\partial y}+\frac{\partial p}{\partial \sigma}\frac{\partial \sigma}{\partial y^*}\right)_{i,j,k}^{n+1}+g_y \tag{16}$$

$$\frac{w_{i,j,k}^{n+1}-w_{i,j,k}^{n+2/3}}{\Delta t}=-\frac{1}{\rho}\left(\frac{\partial p}{\partial \sigma}\frac{\partial \sigma}{\partial z^*}\right)_{i,j,k}^{n+1}+g_z \tag{17}$$

and the continuity Equation (6) is discretized as follows:

$$\left(\frac{\partial u}{\partial x}+\frac{\partial u}{\partial \sigma}\frac{\partial \sigma}{\partial x^*}+\frac{\partial v}{\partial y}+\frac{\partial v}{\partial \sigma}\frac{\partial \sigma}{\partial y^*}+\frac{\partial w}{\partial \sigma}\frac{\partial \sigma}{\partial z^*}\right)_{i,j,k}^{n+1}=0 \tag{18}$$

Performing the following operation:

$$\frac{\partial(15)}{\partial x}+\frac{\partial(15)}{\partial \sigma}\frac{\partial \sigma}{\partial x^*}+\frac{\partial(16)}{\partial y}+\frac{\partial(16)}{\partial \sigma}\frac{\partial \sigma}{\partial y^*}+\frac{\partial(17)}{\partial \sigma}\frac{\partial \sigma}{\partial z^*}$$

and making use of (18), we obtain the modified Poisson pressure equation as follows:

$$\begin{aligned}&\left\{\frac{\partial}{\partial x}\left(\frac{1}{\rho}\frac{\partial p}{\partial x}\right)+\frac{\partial}{\partial y}\left(\frac{1}{\rho}\frac{\partial p}{\partial y}\right)+\left[\left(\frac{\partial \sigma}{\partial x^*}\right)^2+\left(\frac{\partial \sigma}{\partial y^*}\right)^2+\left(\frac{\partial \sigma}{\partial z^*}\right)^2\right]\frac{\partial}{\partial \sigma}\left(\frac{1}{\rho}\frac{\partial p}{\partial \sigma}\right)\right.\\&+\frac{\partial \sigma}{\partial x^*}\left[\frac{\partial}{\partial x}\left(\frac{1}{\rho}\frac{\partial p}{\partial \sigma}\right)+\frac{\partial}{\partial \sigma}\left(\frac{1}{\rho}\frac{\partial p}{\partial x}\right)\right]+\frac{\partial \sigma}{\partial y^*}\left[\frac{\partial}{\partial y}\left(\frac{1}{\rho}\frac{\partial p}{\partial \sigma}\right)+\frac{\partial}{\partial \sigma}\left(\frac{1}{\rho}\frac{\partial p}{\partial y}\right)\right]\\&\left.+\left(\frac{\partial^2 \sigma}{\partial x^* \partial x}+\frac{\partial^2 \sigma}{\partial y^* \partial y}\right)\left(\frac{1}{\rho}\frac{\partial p}{\partial \sigma}\right)\right\}_{i,j,k}^{n+1}\\&=\frac{1}{\Delta t}\left(\frac{\partial u}{\partial x}+\frac{\partial u}{\partial \sigma}\frac{\partial \sigma}{\partial x^*}+\frac{\partial v}{\partial y}+\frac{\partial v}{\partial \sigma}\frac{\partial \sigma}{\partial y^*}+\frac{\partial w}{\partial \sigma}\frac{\partial \sigma}{\partial z^*}\right)_{i,j,k}^{n+2/3}\end{aligned} \tag{19}$$

The left-hand side of (19) differs from that in Reference [15] with the inclusion of density derivative. The finite difference representation can be exemplified by expressing the first term in x-direction:

$$\begin{aligned}\left[\frac{\partial}{\partial x}\left(\frac{1}{\rho}\frac{\partial p}{\partial x}\right)\right]_{i,j,k}^{m}&=\frac{1}{\Delta x}\left[\left(\frac{1}{\rho}\frac{\partial p}{\partial x}\right)_{i+1/2,j,k}-\left(\frac{1}{\rho}\frac{\partial p}{\partial x}\right)_{i-1/2,j,k}\right]^m\\&=\frac{1}{\Delta x}\left[\frac{1}{\rho_{i+1/2,j,k}}\frac{p_{i+1,j,k}-p_{i,j,k}}{\Delta x_i}-\frac{1}{\rho_{i-1/2,j,k}}\frac{p_{i,j,k}-p_{i-1,j,k}}{\Delta x_{i-1}}\right]^m\end{aligned} \tag{20}$$

A sparse matrix will result from (19) with 7 diagonal lines originating from first- and second-order derivatives of pressure and another 8 from second-order cross-differentiations of pressure. The matrix can be solved by the standard matrix solvers as employed by Lin and Li [15], i.e. conjugate gradient (CG) or successive overrelaxation (SOR) method.

3.2.4. Velocity-correction step. After the pressure is updated, it can be substituted into (15)–(17) to obtain the new velocity. For example, the horizontal velocity is obtained as

follows:

$$\frac{u_{i,j,k}^{n+1}-u_{i,j,k}^{n+2/3}}{\Delta t}=-\frac{1}{\rho}\left(\frac{\partial p}{\partial x}+\frac{\partial p}{\partial \sigma}\frac{\partial \sigma}{\partial x^*}\right)_{i,j,k}^{n+1}+g_x$$

$$=-\frac{1}{\Delta x_{i-1}+\Delta x_i}\left(\frac{1}{\rho_{i+1/2,j,k}}\frac{(p_{i+1,j,k}-p_{i,j,k})\Delta x_{i-1}}{\Delta x_i}\right.$$

$$\left.+\frac{1}{\rho_{i-1/2,j,k}}\frac{(p_{i,j,k}-p_{i-1,j,k})\Delta x_i}{\Delta x_{i-1}}\right)$$

$$-\frac{1}{\Delta \sigma_{k-1}+\Delta \sigma_k}\left(\frac{1}{\rho_{i,j,k+1/2}}\frac{(p_{i,j,k+1}-p_{i,j,k})\Delta \sigma_{k-1}}{\Delta \sigma_k}\right.$$

$$\left.+\frac{1}{\rho_{i,j,k-1/2}}\frac{(p_{i,j,k}-p_{i,j,k-1})\Delta \sigma_k}{\Delta \sigma_{k-1}}\right)\frac{\partial \sigma}{\partial x^*}+g_x \tag{21}$$

3.2.5. Density tracking step. After the new velocities are obtained, the transport equation (10) can then be solved. The similar split operator method is used to treat the advection and diffusion terms separately. In this study, the CIP method [16], which gives an accurate solution for front capturing, is used to solve the advection term. The detailed description of CIP method can be referred to the original paper by Yabe *et al.* [16]. The basic finite different form of CIP method in the 1D case is simplified as

$$\rho_{i,j,k}^{n+1}=\left[(a_{i,j,k}\xi+b_{i,j,k})\xi+\left(\frac{\partial \rho}{\partial x}\right)_{i,j,k}^{n}\right]\xi+\rho_{i,j,k}^{n}$$

$$\left(\frac{\partial \rho}{\partial x}\right)_{i,j,k}^{n+1}=(3a_{i,j,k}\xi+2b_{i,j,k})\xi+\left(\frac{\partial \rho}{\partial x}\right)_{i,j,k}^{n} \tag{22}$$

where $\xi=-u_{i,j,k}\Delta t$. The coefficients $a_{i,j,k}$ and $b_{i,j,k}$ in Equation (22) are determined from the continuities of $\rho_{i,j,k}$ and its spatial derivatives $(\partial\rho/\partial x)_{i,j,k}^{n}$ at grid points.

3.2.6. Free surface tracking step. Finally, the free surface displacement is updated by solving Equation (12). The finite difference form is as follows:

$$\frac{\eta_{i,j,k}^{n+1}-\eta_{i,j,k}^{n}}{\Delta t}=-\frac{1}{\Delta x_{i-1}+\Delta x_i}\left(\Delta x_{i-1}\frac{FX_{i+1,j,k}-FX_{i,j,k}}{\Delta x_i}+\Delta x_i\frac{FX_{i,j,k}-FX_{i-1,j,k}}{\Delta x_{i-1}}\right)$$

$$-\frac{1}{\Delta y_{j-1}+\Delta y_j}\left(\Delta y_{j-1}\frac{FY_{i,j+1,k}-FY_{i,j,k}}{\Delta y_j}+\Delta y_j\frac{FY_{i,j,k}-FY_{i,j-1,k}}{\Delta y_{j-1}}\right) \tag{23}$$

where FX and FY are the momentum fluxes in x- and y-directions, and their finite difference forms have been detailed in Reference [15].

4. MODEL VERIFICATION

4.1. Additional convective effect in a stratified flow

Consider the following 1D diffusion problem with a spatially variable density, which is simplified from Equation (7) by neglecting the convection, pressure and body force in a 1D untransformed domain:

$$\frac{\partial u(x,t)}{\partial t} = \frac{1}{\rho(x)} \frac{\partial}{\partial x} \left[2\nu\rho(x) \frac{\partial u(x,t)}{\partial x} \right] \tag{24}$$

In the above problem, the density is assumed to vary with space only. Differentiating the above equation by parts, we obtain

$$\frac{\partial u(x,t)}{\partial t} - c(x)\frac{\partial u(x,t)}{\partial x} = 2\nu \frac{\partial^2 u(x,t)}{\partial x^2} \tag{25}$$

where $c(x) = [2\nu/\rho(x)][\partial\rho(x)/\partial x]$. It is seen that the original diffusion problem with a variable density is equivalent to a convection–diffusion problem with the convective velocity being the function of ν, ρ and $\partial\rho/\partial x$. Equation (25) has analytical solutions for some simple initial and boundary conditions. For example, under the following initial and boundary conditions:

$$\text{IC} \begin{cases} u(x,0) = 0 & \text{at } -\infty \leqslant x \leqslant 0 \\ u(x,0) = u_0 = 1 & \text{at } 0 \leqslant x \leqslant +\infty \end{cases} \qquad \text{BC} \begin{cases} u(-\infty,t) = 0 \\ u(+\infty,t) = 1 \end{cases}$$

the analytical solution to Equation (25) can be found as

$$u(x,t) = u_0 \left\{ 1 - \frac{1}{2} \, erfc \left[\frac{x + c(x)t}{2\sqrt{\nu t}} \right] \right\} \tag{26}$$

In this test, the fluid density is taken to be $\rho(x) = 1000 + 25x$ (kg/m^3), and the density gradient is thus a constant $[\partial\rho(x)]/\partial x = 25\,\text{kg/m}^4$. The kinematic viscosity is set to $\nu = 1.0\,\text{m}^2/\text{s}$.

Equation (25) is solved by using the present model in a finite domain of $-20\,\text{m} \leqslant x \leqslant 20\,\text{m}$. The computation has been carried out up to 20 s. The numerical results are compared to analytical solutions in Figure 1. We have observed that the model is in good agreement with the exact solution. Both the numerical results and analytical solution show that the centre of profile ($u = 0.5\,\text{m/s}$) moves to left due to the additional convective process induced by density variation.

4.2. Horizontal density-gradient flow

In this section, a horizontal density-driven flow is simulated. Considering a 2D flow whose density is a linear function of x only, i.e. $\partial\rho/\partial x = \lambda$, where λ is a constant, the governing

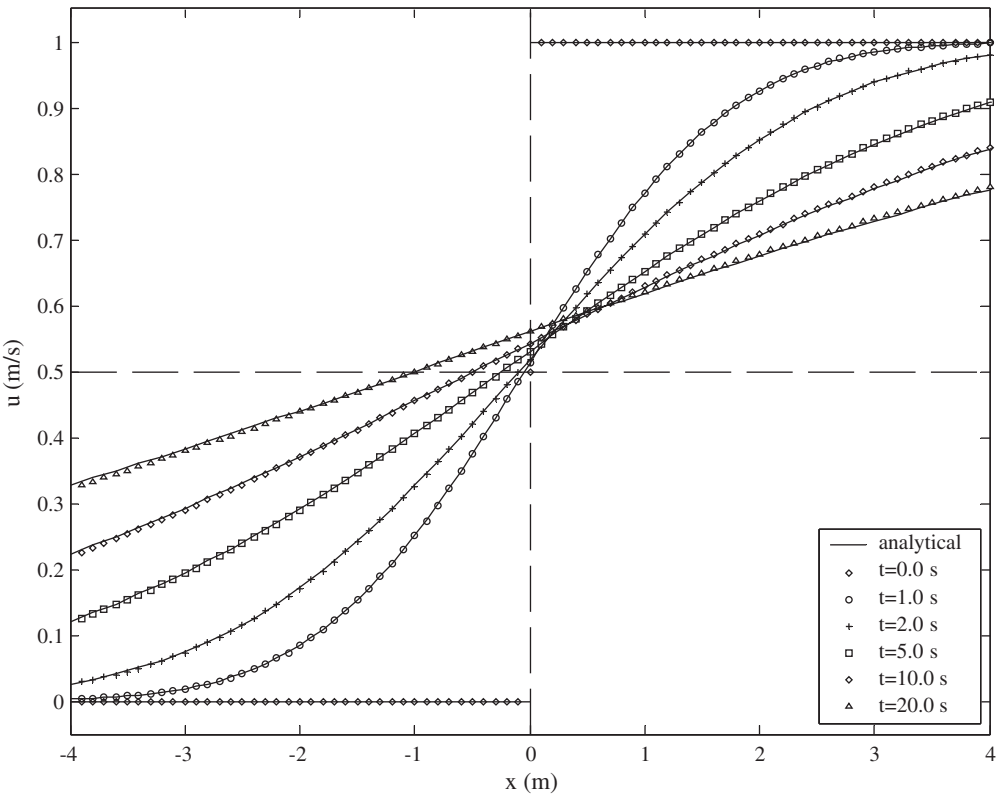

Figure 1. Comparisons of numerical velocity profile at $t = 1, 2, 5, 10, 20$ s with analytical solution.

equation (7) in an untransformed domain can be reduced to

$$\frac{1}{\rho}\frac{\partial p}{\partial x} = v_z \frac{\partial^2 u}{\partial z^2} \tag{27}$$

where v_z is the vertical diffusivity. This is a simplified case of estuarial flow driven by salinity gradient (see Figure 2). When the run-off and bottom friction are neglected, Officer [18] gave the analytical expression for the horizontal velocity as the function of z:

$$u(z) = \frac{1}{24}\frac{g\lambda h^3}{\rho v_z}\left[1 - 6\left(\frac{z}{h}\right)^2 + 4\left(\frac{z}{h}\right)^3\right] \tag{28}$$

In this test, the following values are used: $v_z = 0.005$ m^2/s, $h = 20$ m, $\lambda = 1$ kg/m^3/km, $\rho = 1025$ kg/m^3, and the basin has a length of $L = 20$ km. The numerical simulation was performed by using 20 meshes in vertical direction and 20 meshes in horizontal direction. The numerical results at the steady state are shown in Figure 3. Very good comparisons are obtained between numerical results and analytical solution.

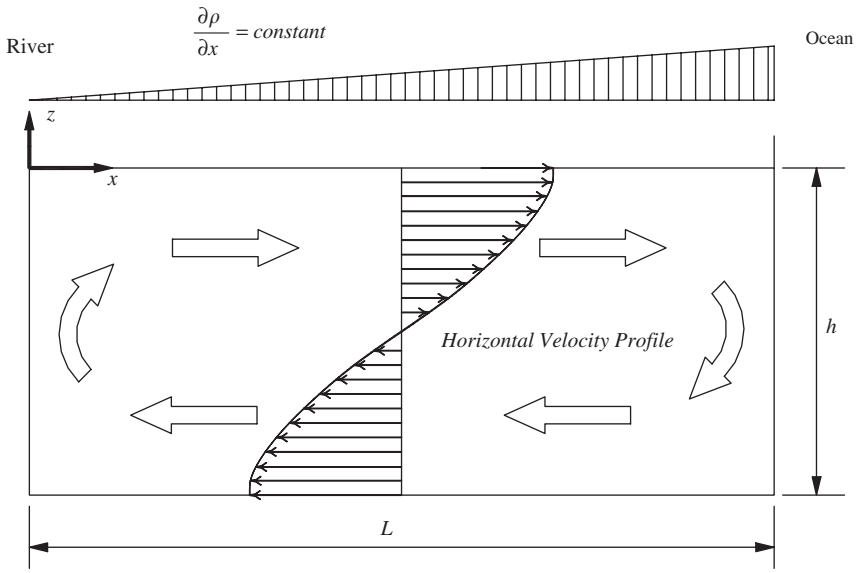

Figure 2. Schematic diagram of density-driven flow in a tank.

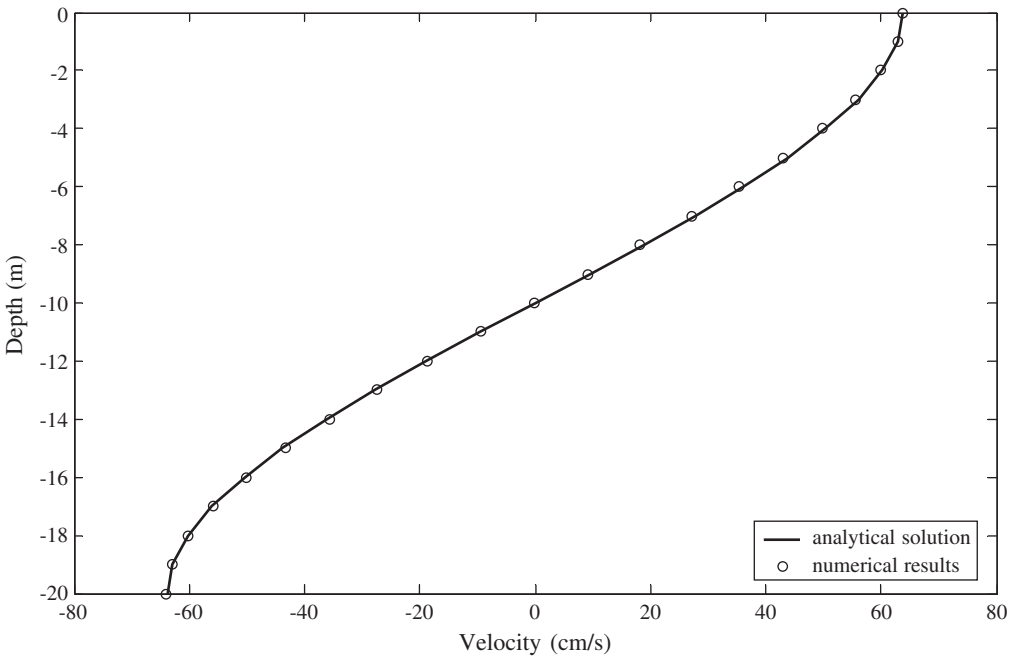

Figure 3. Comparisons of velocity profile between numerical results and analytical solution for a horizontal density-gradient flow.

5. CASE STUDIES

5.1. Background of sediment dumping

Ocean disposal of dredged material is a common practice after the dredging of navigation channels and harbours, or during the construction of breakwaters as well as land reclamation. The accurate prediction of settling processes of disposed material in open waters, such as descending, transport and dispersion of the material, is of practical importance for both engineering management and environmental protection.

A few experimental studies on particle thermals were performed by Murota *et al.* [19], Nakatsuji *et al.* [20], Tamai *et al.* [21] and Bühler and Papantoniou [22]. Nakatsuji *et al.* [20] found that the dynamic behaviour of a sand cloud is close to the heavy thermal motion and the plane particle clouds approached a constant frontal velocity in their final stage. The particles move independently and motion is dominated by the balance between the buoyant force and the drag force on each particle with relatively large particle sizes. Bühler and Papantoniou [22] suggested that suspension thermals eventually evolve into particle swarms, which descend at a constant velocity, and grow slightly in size along the path. They proposed that the ratio of the square root of the initial buoyancy flux to the settling velocity is a characteristic length scale in flow transition stage from a suspension thermal to a particle swarm.

To better understand those mechanisms, a number of researchers investigated the dumping process numerically. Oda and Shigematsu [23] analysed the 2D descent and dispersion behaviours of soil particles in still waters by a Combined-DEM-MAC method, which coupled two numerical methods in order to consider the initial condition and the interaction between particles and fluid flow. Li [9] performed numerical experiments of dynamic motions of dumping particles from initial particle thermal to the swarm stage. By assuming the discrete particles can be represented by a continuous density fluid, the approach produced satisfactory results against experimental measurements. Boussinesq assumption was applied in the above numerical model.

In this study, the present numerical model is applied to investigate the dumping process. To verify the numerical model, comparisons will be made between numerical results and available experimental data by Murota *et al.* [19] and Nakatsuji *et al.* [20] for both coarse and medium-size sediments in 2D cases. The model will then be used to study 3D sediment dumping problems with the presence of free surfaces. The physical phenomena of free surface deformation and radial spreading of the sediment clouds will be examined.

5.2. Determination of physical parameters

5.2.1. Drift velocity. The drift velocity in Equation (3) is the result of separation of suspended particle from its ambient flow. Apparently, for an extreme case of mean fluid density being equal to particle density (this may never happen in reality no matter how compact the particles are due to the finite value of porosity), this drift velocity equals zero because its vertical motion can be fully governed by the local density gradient. On the other hand, for a very dilute flow where the mean density gradient is negligible, this drift velocity will approach to the settling velocity of individual solid particle because every solid particle settles down by its own net weight regardless of the nearby mean fluid density gradient. Therefore, the drift velocity is in principle the function of local density. In this study, however, for the simplicity

of the treatment and the consideration of the fact that the sediment plume will quickly spread out after the release, we decide to approximate the drift velocity by the settling velocity of individual sediment:

$$w_d = V_s = \sqrt{\frac{4g}{3C_D}\frac{\rho_s - \rho_a}{\rho_a}d} \tag{29}$$

where $\rho_s = 2650\,\mathrm{kg/m^3}$ is the density of the particle, $\rho_a = 1000\,\mathrm{kg/m^3}$ is the density of ambient water, d is the diameter of the particle and C_D indicates the drag coefficient which for spherical particles is expressed as [24]

$$\begin{aligned} C_D &= \frac{24}{Re}(1 + 0.1315Re^{0.82-0.05\,\log_{10}Re}) \quad 0.01 < Re \leqslant 20 \\ C_D &= \frac{24}{Re}(1 + 0.1935Re^{0.6305}) \qquad\qquad 20 \leqslant Re \leqslant 260 \end{aligned} \tag{30}$$

We shall realize that by adapting the above treatment, the downward motion of the sediment plume can be overestimated in the early stage when the mean fluid density is still significant; this will be further discussed in the following simulations.

5.2.2. Eddy viscosity. The proper choice of eddy viscosity model is very important in order to predict the correct spreading rate of sediment plume. In this study, the simple mixing-length hypothesis neglecting again the density effect is used to determine the eddy viscosity in Equation (2). Following Rodi [25], the expression of the eddy viscosity ν_t is

$$\nu_t = l_m^2 \left[\left(\frac{\partial u_i}{\partial x_j} + \frac{\partial u_j}{\partial x_i}\right)\frac{\partial u_i}{\partial x_j}\right]^{1/2} \tag{31}$$

where the mixing length l_m is calculated by $l_m = Cb$ with b being defined as the normal length (half width) of the cloud (see Figure 4). In the computation, b changes with time and it measures from the centre of the cloud to its outermost edge where the local density $\rho = \rho_a + 0.1(\rho_{max} - \rho_a)$ with ρ_{max} being the maximal density in the entire domain at that instance. $C = 0.09$ is the mixing length coefficient. The Schmidt number is set to 1.0 that renders $\Gamma_t = \nu_t$ in Equation (3).

5.3. Numerical experiments for 2D cases

The present numerical model has been applied to predict the settling behaviour and deposition configuration of sediments dumped into a water tank as shown in Figure 4. The computational conditions follow those in the experiment conducted by Murota *et al.* [19] and Nakatsuji *et al.* [20]. In this study, we simulated sediments with three mean diameters, namely, $d_{50} = 0.8\,\mathrm{mm}$ (medium-size), 1.3 mm (medium-size) and 5.0 mm (coarse). The computational domain is chosen to be $1\,\mathrm{m} \times 1\,\mathrm{m}$ that is discretized by a uniform mess system of 100×100. The initial volume of particles is chosen to be $q_0 = 5\,\mathrm{cm^2}$ in Case 1 for the study of falling velocity of the sediment cloud and $q_0 = 10\,\mathrm{cm^2}$ in Case 2 for the study of spreading rate.

The comparisons of calculated results and experimental data for the falling velocity of the particle cloud are displayed in Figure 5 for both coarse and medium-size sediments. In this figure the falling velocity of the particle cloud W_c, which is defined as the velocity of the

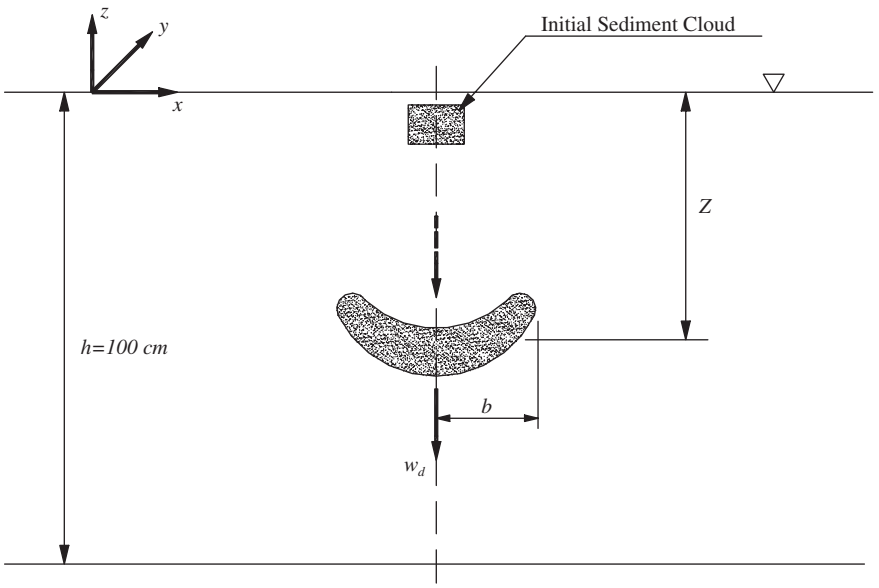

Figure 4. Illustration of sediment dumping.

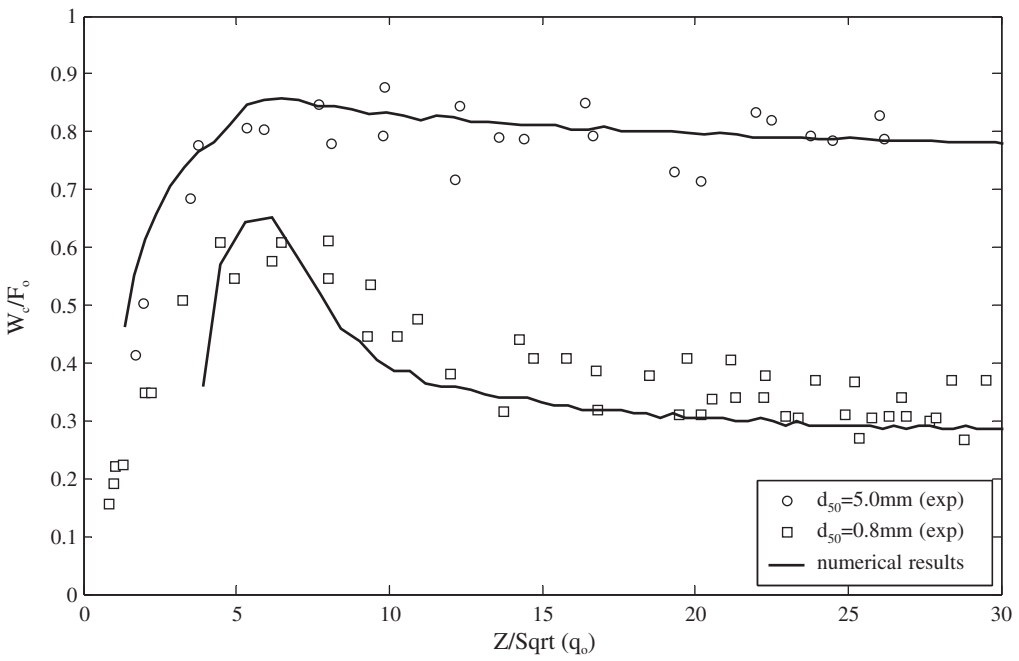

Figure 5. Comparisons of falling velocities of the sediment clouds as the function of settling distance for Case 1 ($q_0 = 5\,\mathrm{cm}^2$).

centroid of the sediment cloud, is normalized by the characteristic velocity based on buoyancy flux $F_0 = \sqrt{g\sqrt{q_0}\Delta\rho/\rho}$ where $\Delta\rho = \rho_c - \rho_a$ is the initial density difference between the particle cloud (ρ_c) and the ambient water (ρ_a). In the following simulation, the porosity of sediment is set to $\theta = 0.394$ that makes $\rho_c = 2000\,\mathrm{kg/m^3}$. The settling distance Z is measured from the free surface downward to the centroid of the sediment cloud and it is normalized by the square root of q_0 in Figure 5. For larger $d_{50} = 5.0\,\mathrm{mm}$, the falling velocity of the cloud quickly approached a constant value that is close to the settling velocity of individual particles in calm water. For smaller $d_{50} = 0.8\,\mathrm{mm}$ the dynamic behaviour of the sediment cloud is similar to thermal motion. The falling velocity of the cloud accelerates first and then reduces gradually. The acceleration of the cloud has been overestimated in the early stage when the mean density is still high because of the overestimation of actual drift velocity in (29) with the use of settling velocity. For finer sediments, it takes much longer time for the sediment cloud to reach the constant value of the settling velocity.

The spreading width $R_c = 2b$ of the sediment clouds is investigated in Case 2 and presented in Figure 6. The numerical results are in fair agreement with the experimental data. Both numerical and experimental results show that the larger the particle size, is, the smaller the spreading rate of the cloud. Further inspection shows that the width of the cloud varies nearly linearly with the settling distance for smaller sediments, while it bends slightly inward for larger sediments. We shall provide qualitative explanation for this phenomenon later when we examine the detailed velocity field for the 3D sediment dumping problems.

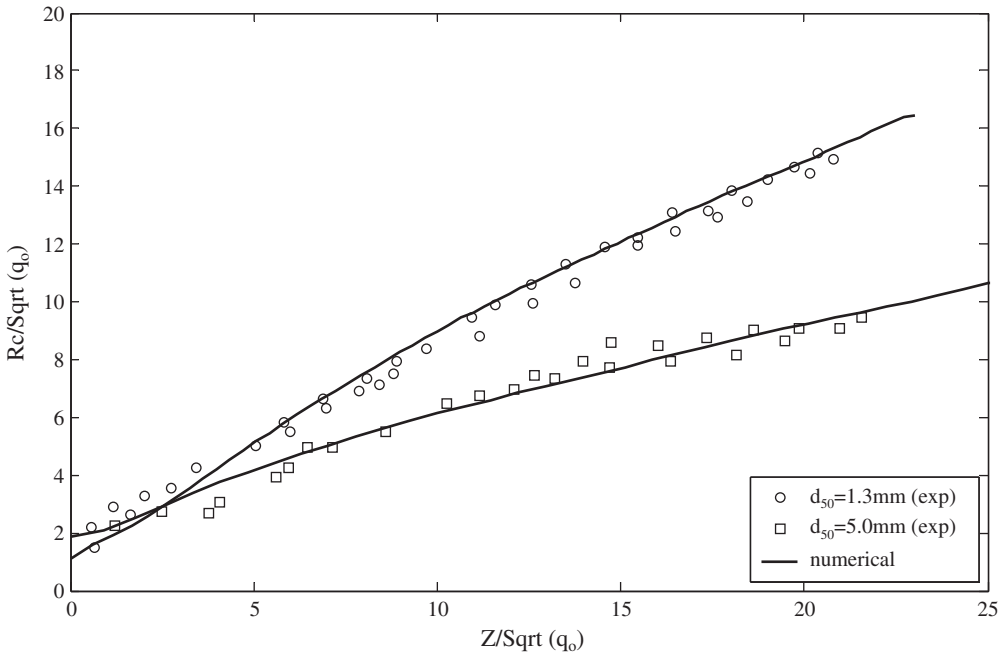

Figure 6. Comparisons of spreading width of the sediment clouds as the function of settling distance for Case 2 ($q_0 = 10\,\mathrm{cm^2}$).

5.4. 3D sediment dumping

In this section, a 3D simulation is conducted to investigate sediment dumping in a water body where free surface is present. The sketch of the problem is similar to Figure 4 except that the initial sediments have a cubic shape. The computational region is $0.80\,\mathrm{m} \times 0.80\,\mathrm{m} \times 1.00\,\mathrm{m}$ that is discretized by $80 \times 80 \times 100$ uniform grids. The initial sediment cloud is introduced at the centre of the upper surface, and it has a volume of $3\,\mathrm{cm} \times 3\,\mathrm{cm} \times 3\,\mathrm{cm}$.

Two typical cases have been simulated, one with medium-size particles (e.g. $d_{50} = 1.3\,\mathrm{mm}$) and the other fine particles (e.g. $d_{50} = 0.15\,\mathrm{mm}$). Figures 7 and 8 showed the simulated results of free surface profiles and isosurfaces of density fields. The free surface displacement has been magnified in Figures 7 and 8 for better visualization. It is observed that the free surface is pulled down initially when sediments are just released ($t = 0.1$ s) and it comes up later when the sediment clouds move deeper and the ambient water returns to fill up the space ($t = 0.4$ s). Free surfaces gradually calm down when sediments go even deeper ($t = 1.0$ s). For fine sediments, a toroid-shape cloud is formed during the descent process; whereas, a plate-like cloud with smaller diameter is created for medium-size sediments ($t = 3.0$ s). This phenomenon will be explained below by examining the detailed velocity fields associated with the sediment clouds.

The velocity fields and density contours at the central cross-sections are shown in Figure 9 for fine sediments and Figure 10 for medium-size sediments. For fine sediments, the

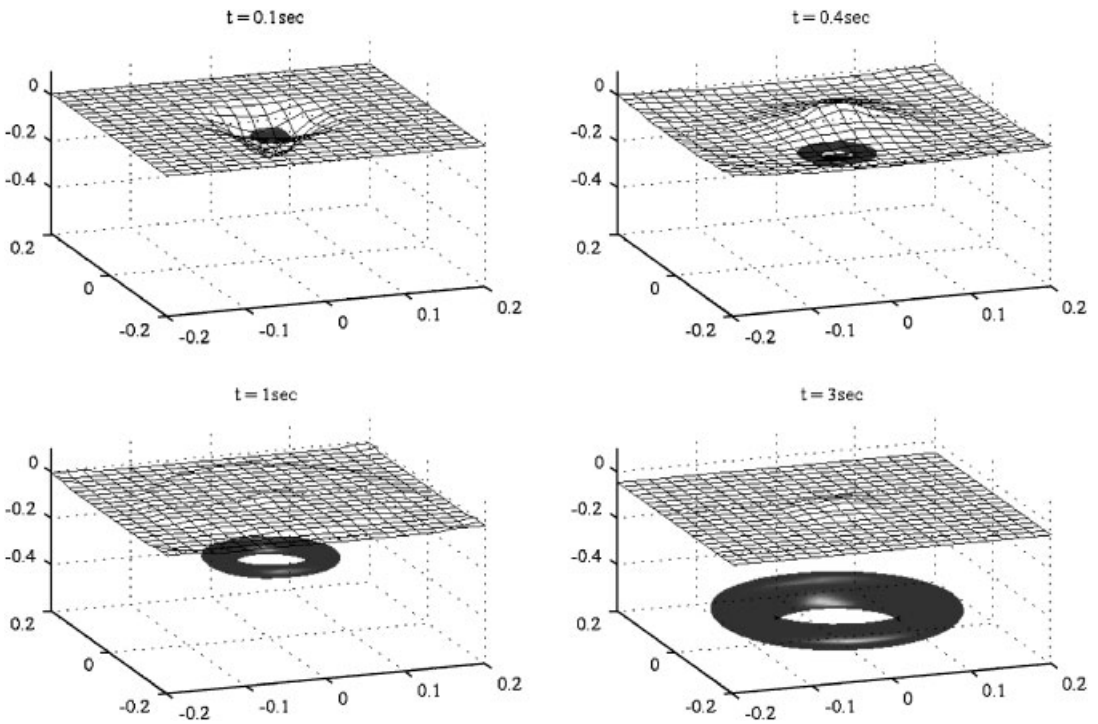

Figure 7. Free surface profiles and density isosurfaces (average of maximal and minimal fluid density) for fine sediments at $t = 0.1$, 0.4, 1.0, 3.0 (s).

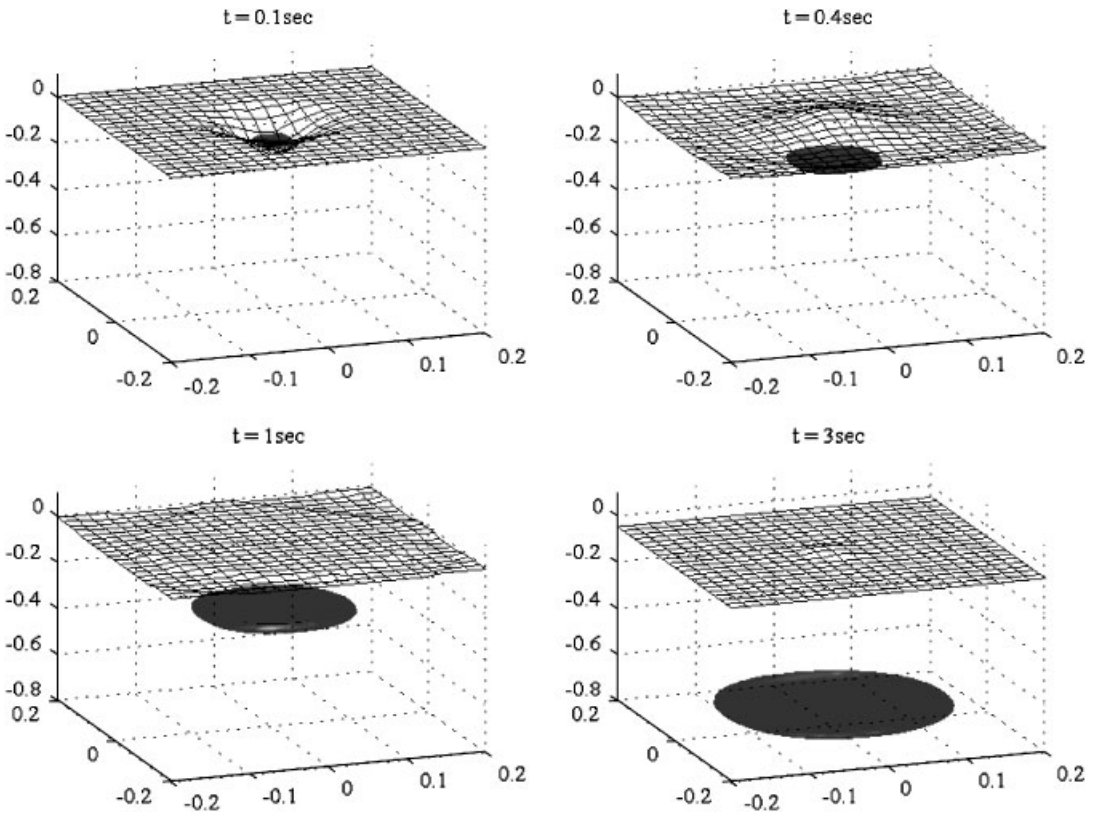

Figure 8. Free surface profiles and density isosurfaces (average of maximal and minimal fluid density) for medium-size sediment at $t = 0.1$, 0.4, 1.0, 3.0 (s).

generation of vortex pair is found to be similar to that in Reference [9]. The density field has its maxima located near the pair of vortex centres. As a result, the sediment motion follows closely to the vortical fluid motion, which tears down the sediment cloud and forces the sediments to spread out in its radial direction. Such vortex-induced radial motion can persist for rather long time even after the sediment cloud reaches the bottom and it is responsible for the formation of the so-called density current that have been frequently reported by field measurements. For example, Drapeau *et al.* [26] found that for very fine sediments (e.g. $d_{50} = 0.063\text{mm}$), density currents had significant values even minutes after the sediment clouds reached the seabed, making the dumped sediments expand radially and form a shape of tore.

For medium-size particles, however, the phenomenon of vortex pair is not apparent and the double peaks in density field disappear. This is due to the fact that larger sediments have larger settling velocity, which makes the sediment cloud move away from vortex centres before the vortex pair is fully developed. Subsequently, the particles will be less affected by the vortical fluid motion, which has been already weakened. The corresponding cloud spreading in radial direction is therefore smaller. As a result, the sediment cloud remains to be plate-like during

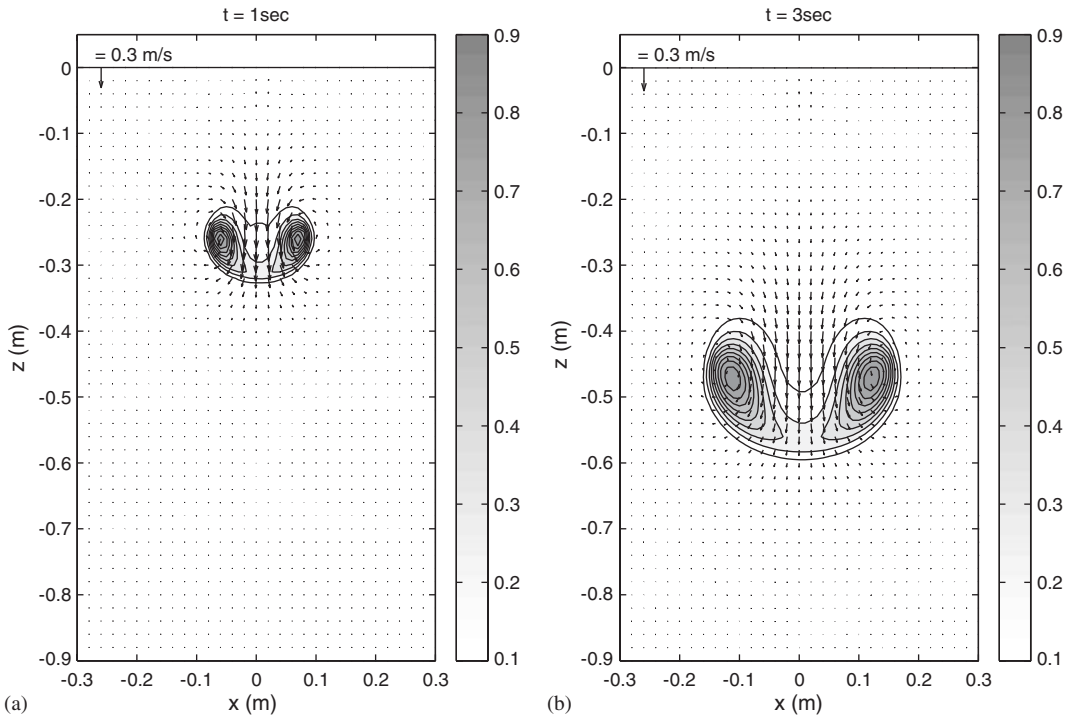

Figure 9. Velocity fields and density contours (at the intervals of 1/10 of density difference) at the central cross-section for fine sediments.

the descending process. This also explains why in Figure 6 the spreading width for larger sediments is smaller and tends to bend inward.

6. CONCLUSION

In this study, a 3D numerical model for simulating stratified free surface flows has been developed based on the original 3D Reynolds-averaged Navier–Stokes (RANS) equations. The model is the extension of an earlier σ-coordinate model [15] by including additional density variation. The new model has been validated for the 1D diffusion problem and 2D density-gradient flow. Excellent agreements have been obtained between the computed results and analytical solutions. It is found that the diffusion of the density stratified flow will result in an additional flow advection.

The model is further used to study the sediment dumping into water, which is modelled as a strongly stratified flow. While the drift velocity is obtained approximately by the settling velocity with the exclusion of density effects, the eddy viscosity is also modelled by the simple mixing-length hypothesis without the consideration of density variation. For the 2D cases where experimental results are available, numerical experiments are conducted for sediments with medium and large sizes. Good comparisons are obtained for both types of sediments in

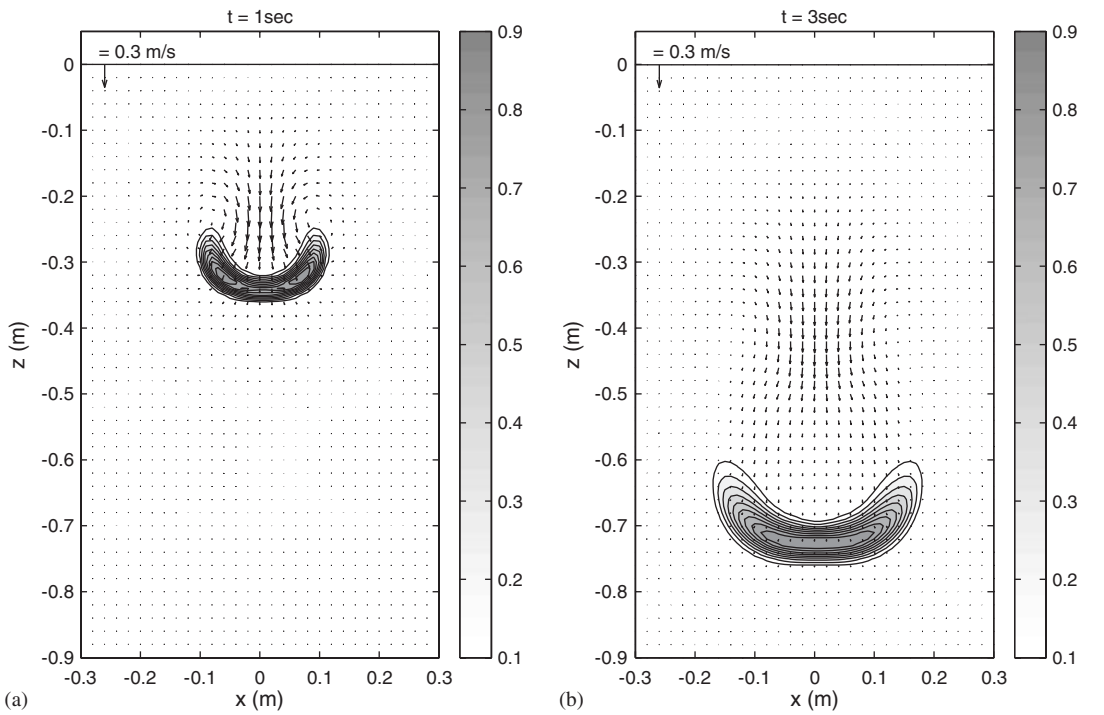

Figure 10. Velocity fields and density contours (at the intervals of 1/10 of density difference) at the central cross-section for medium-size sediments.

terms of falling velocity and spreading rate of the sediment clouds except that the downward motion has been overestimated in the early stage of dumping due to the double accounts for the density variation and settling velocity. The model is finally employed to investigate the 3D sediment dumping in the presence of free surface deformation. Reasonable results have been obtained in terms of free surface motion as well as the descending and spreading of the sediments clouds. It is found that during the descent an annulus-like cloud will be formed for fine sediments whereas a plate-like cloud for sediments with medium size.

The present model has proven to be an accurate tool for studying free surface flows with strong density stratification such as sediment dumping, for which the conventional Boussinesq assumption may not be valid. Future works, however, are still necessary for the more appropriate definition of the drift velocity and eddy viscosity with the consideration of local density effects. The individual contribution from the dynamic pressure and the actual density stratification without Boussinesq assumption will also be quantified and studied in the future.

ACKNOWLEDGEMENTS

The work is supported, in part, by the research fund from the National University of Singapore (WBS: R-264-000-136-112).

REFERENCES

1. Rubin H, Atkinson J. *Environmental Fluid Mechanics*. Marcel Dekker: New York, 2001.
2. Ricou FP, Spalding DB. Measurements of entrainment by axisymmetrical turbulent jets. *Journal of Fluid Mechanics* 1961; **8**:21–32.
3. Woods AW. A note on non-Boussinesq plumes in an incompressible stratified environment. *Journal of Fluid Mechanics* 1997; **345**:347–356.
4. Gu R. Numerical simulation of 2D buoyant jets in ice-covered and temperature stratified water. *Advances in Water Resources* 1998; **21**:363–373.
5. Liu WC, Hsu MH, Kuo AY. Application of different turbulence closure model for stratified tidal flows and salinity in an estuarine system. *Mathematics and Computers in Simulation* 2002; **59**:437–451.
6. Shen YM, Ng CO, Chwang AT. A two-fluid model of turbulent two-phase flow for simulating turbulent stratified flows. *Ocean Engineering* 2003; **30**:153–161.
7. Huang W, Spaulding M. 3D Model of estuarine circulation and surface discharges. *Journal of Hydraulic Engineering* (ASCE) 1995; **121**(4):300–311.
8. Fung YT, Chang WS. Surface and internal signatures of organized vortex motions in stratified fluids. *Physics of Fluids* 1996; **8**(11):3023–3056.
9. Li CW. Convection of particle thermals. *Journal of Hydraulic Research* 1997; **35**(3):355–376.
10. Paisley MF, Bhatti NM. Comparison of multigrid methods for neutral and stably stratified flows over two-dimensional obstacles. *Journal of Computational Physics* 1998; **142**:581–610.
11. Galmiche M, Hunt JCR, Thual O, Bonneton P. Turbulence-mean field interactions and layer formation in a stratified fluid. *European Journal of Mechanics B—Fluids* 2001; **20**:577–585.
12. Torres CR, Ochoa J, Castillo J, Van Woert M. Initial flow field of stratified flow past an impulsively started sphere. *Applied Numerical Mathematics* 2002; **40**:235–244.
13. Blumberg AF, Mellor GL. A description of a three-dimensional coastal ocean circulation model (POM). *Three-Dimensional Coastal Ocean Models*, vol. 4. American Geophysical Union: Washington, DC, 1987.
14. Xing J, Davies AM. Processes influencing the circulation and bottom mixing across the shelf slope: the importance of the slope topography and the coast. *Journal of Marine Systems* 1999; **21**:341–377.
15. Lin P, Li CW. A σ-coordinate three-dimensional numerical model for surface wave propagation. *International Journal for Numerical Methods in Fluids* 2002; **38**:1045–1068.
16. Yabe T, Ishikawa T, Wang PY, Aoki T. A universal solver for hyperbolic equations by cubic-polynomial interpolation II. Two- and three-dimensional solvers. *Computer Physics Communications* 1991; **66**:233–242.
17. Blumberg AF, Mellor GL. Diagnostic and prognostic numerical circulation studies of the South Atlantic Bight. *Journal of Geophysical Research* 1983; **88**(C8):4579–4592.
18. Officer CB. *Physical Oceanography of Estuaries* (*and Associated Coastal Waters*). Wiley: New York, 1976.
19. Murota A, Nakatsuji K, Tamai M, Machida H. Formation of solid-and-fluid buoyancy cloud in reclining works. *Proceedings of the 35th Japanese Conference on Coastal Engineering*, 1998; 777–781.
20. Nakatsuji K, Tamai M, Murota A. Dynamic behaviours of sand clouds in water. *International Conference on Physics Modelling of Transport and Dispersion*, M.I.T. Boston, 8C.1, 1990.
21. Tamai M, Muraoka K, Murota A. Diffusion process of turbidity in direct dumping of soil. In *Environmental Hydraulics*, Lee, Cheung (eds), vol. 1. Balkema: Rotterdam, 1991; 147–152.
22. Bühler J, Papantoniou DA. Swarms of coarse particles falling through a fluid. In *Environmental Hydraulics*, Lee, Cheung (eds), vol. 1. Balkema: Rotterdam, 1991; 135–140.
23. Oda K, Shigematsu T. Development of a numerical simulation method for predicting the settling behavior and deposition configuration of soil dumped into waters. *Proceedings of the 24th International Conference on Coastal Engineering*, vol. III, Chapter 238, ASCE, Japan, 1994; 3305–3319.
24. Clift R, Grace JR, Weber ME. *Bubbles*, *Drops*, *and Particles*. Academic Press: New York, 1978; 112.
25. Rodi W. *Turbulence Models and Their Application in Hydraulics—a State of the Art Review*. IAHR: Netherlands, 1984.
26. Drapeau G, Gauthier D, Lavallee D. *In situ* deposition versus transport by density currents of dredged sediments dumped in coastal waters. *Journal of Coastal Research* 1999; **15**(1):87–96.

